RSC Advances

PAPER

View Article Online
View Journal | View Issue

Cite this: *RSC Adv.*, 2024, **14**, 38459

Novel polyvinyl alcohol-assisted MnO_2–ZnO–CuO nanocomposites as an efficient photocatalyst for methylene blue degradation from wastewater†

Teketel Girma Gindose, [ab] Gebrehiwot Gebreslassie, [abe] Tessema Derbe Hailegebreal, [abd] Tesfay G. Ashebr, [ab] Fanyana Mtunzi, [f] Tsegaye Belege Atisme [ab] and Enyew Amare Zereffa [*c]

Pristine ZnO (Z), MnO_2 (M), CuO (C) photocatalysts and polyvinyl alcohol (PVA)-assisted MnO_2–ZnO–CuO (MZC) nanocomposites were synthesized *via* the sol–gel method. The synthesized samples were characterized using thermal analysis (TGA), X-ray diffraction (XRD), dynamic light scattering (DLS), scanning electron microscopy (SEM), energy dispersive X-ray (EDS), transmission electron microscopy (TEM), and high-resolution transmission electron microscopy (HRTEM) techniques. The thermal analysis results of the prepared nanomaterial confirmed that the suitable calcination temperature for the synthesis of these nanomaterials is 420 °C. In addition to the morphological and elemental composition, the characteristic diffraction peaks of the MZC nanomaterial were found to align with those of the pristine Z, M, and C photocatalysts. The photocatalytic activities of the synthesized nanomaterials for methylene blue (MB) degradation were evaluated under optimized conditions. The degradation efficiencies of Z, M, C, and MZC were found to be 45%, 57%, 66%, and 93%, respectively, for MB in 180 minutes. The MZC nanocomposite exhibited superior photocatalytic activity compared to the pristine materials, which is attributed to the synergetic effect of the Z, M, and C photocatalysts. The effects of pH, initial dye concentration, and catalyst load were also explored to determine the optimum conditions. The best photocatalytic efficiency was observed at pH 8, with a 130 mg L^{-1} catalyst load, and a 10 mg L^{-1} initial dye concentration. The efficiency of the MZC nanocomposite in real textile wastewater was also tested, achieving 80% degradation of pollutants within 180 minutes. Recycling experiments were conducted for four consecutive cycles under optimal conditions. The photodegradation efficiency for the first, second, third, and fourth cycles was 93%, 91%, 90%, and 89%, respectively, demonstrating high consistency in photodegradation performance across the four cycles. Moreover, a Z-scheme photocatalytic mechanism was proposed as a potential mechanism for the MZC photocatalytic system.

Received 7th September 2024
Accepted 9th November 2024

DOI: 10.1039/d4ra06476c

rsc.li/rsc-advances

1. Introduction

Environmental pollution is a major concern due to the extensive use of organic dyes, colorants, and other coloring products in various industries.[1,2] Specifically, textile factories consume large quantities of organic dyes.[3] Annually, approximately 700 000 tons of dyes are produced, with around 40% being released into water bodies as wastewater from textile factories.[4] This industrial waste contains several hazardous pollutants that pose substantial risks to human health.[5] Among the various dyes found in industrial waste, methylene blue (MB) is widely used for coloring materials such as silk, wool, cotton, and paper.[3,6] However, it is important to note that MB is toxic, tumorigenic, mutagenic, and non-biodegradable, making it a major environmental pollutant.[7,8] Moreover, the presence of MB dye in wastewater is hazardous to aquatic life as it hinders sunlight penetration into the water.[9] Therefore, the removal of dyes before they are released into water bodies is a critical concern.[4,10] Various methods are being investigated for treating wastewater, including coagulation,[9] precipitation,[7] reverse osmosis,[11] and photodegradation using light exposure.[12,13] Among these methods, semiconductor-based photocatalytic

[a]*Department of Industrial Chemistry, Addis Ababa Science and Technology University, P. O. Box 16417, Addis Ababa, Ethiopia*
[b]*Nanotechnology Centre of Excellence, Addis Ababa Science and Technology University, P. O. Box 1647, Addis Ababa, Ethiopia*
[c]*Department of Applied Chemistry, School of Applied Natural Science, Adama Science and Technology University, P. O. Box 1888, Adama, Ethiopia. E-mail: eneyew.amare@astu.edu.et*
[d]*Department of Chemistry, Wachemo University, P. O. Box 667, Hossana, Ethiopia*
[e]*School of Mechanical and Electrical Engineering, University of Electronic Science and Technology of China, Chengdu 611731, China*
[f]*Department of Biotechnology and Chemistry, Vaal University of Technology, Moshoeshoe Road, Sebokengn 1983, South Africa*

† Electronic supplementary information (ESI) available. See DOI: https://doi.org/10.1039/d4ra06476c

degradation has gained attention as an effective approach due to its affordability, simplicity, and environmental benefits.[14,15]

Recently, many researchers have been interested in exploring the photocatalytic activities of semiconductors for the degradation of MB.[15,16] Metal oxide semiconductors, such as MnO_2,[4] CuO,[17] ZnO,[4,7] TiO_2,[18] and Cu_2O,[19] have been extensively studied. Among these semiconductors, ZnO nanoparticles have gained substantial attention due to their versatile applications.[20] However, ZnO has limitations, such as a wide band gap,[7,21] quick recombination of electron–hole pairs, low charge migration efficiency to redox sites,[4] and limited surface reactions to generate reactive species.[20,22] To improve the photocatalytic efficiency of ZnO, it is crucial to enhance the light absorption, optimize the charge separation, increase the surface area, and address the surface mismatch.[22,23] One approach is to create heterostructures by doping ZnO with a metal [24] or non-metal,[25] and integrating ZnO with narrow band gap semiconductors like MnO_2.[22,26] Researchers have achieved effective charge separation by studying the multiphase components of ZnO-based heterojunctions.[27,28] Thus, CuO and MnO_2 semiconductors have been chosen based on their band gap, light absorptivity in the visible region, availability, stability, and non-toxicity for modifying the chemistry of ZnO.[29,30]

Many researchers have studied various three-phase ZnO-based heterostructures, such as ZnO–ZnS–MnO_2,[4] Ag_3PO_4–ZnO–Cu_2O,[7] Cu_2O–ZnO–g-C_3N_4,[31] and ZnO–V_2O_3–WO_3.[32] These heterostructures have shown superior efficiency compared to single ZnO. For instance, J. P. Shubha *et al.*[33] found that the ternary Mn_3O_4–ZnO–Eu_2O_3 photocatalyst exhibited admirable degradation performances of 98% for MB and 96% for methyl orange (MO) within 150 min under natural sunlight irradiation. Many researchers have also successfully developed binary, ternary, and a few quaternary systems of ZnO-based heterojunction nanocomposites for photocatalytic applications.[34,35] However, nanocomposites tend to agglomerate or aggregate, which diminishes their performance in the degradation of dyes.[36,37] To overcome this problem, the use of polymers has gained increasing attention. Among several polymers, polyvinyl alcohol (PVA) has been presented as a viable option owing to its biocompatibility, non-toxicity, biodegradability, water solubility, low calcination temperature, and low thermal stability.[36,38,39]

B. Abebe and coworkers have published a few articles on the use of PVA-assisted ZnO-based binary and ternary nanocomposites to improve the photocatalytic effectiveness of ZnO.[37,39] The results showed the superior catalytic ability of the mixed composite compared to its single ZnO photocatalyst. In spite of these experimental works, research studies associated with the use of mixed-phase composites for photocatalytic applications are far from mature. To the best of the researchers' knowledge, no information is available on the synthesis of mixed-phase MZC nanocomposites for the photodegradation of MB. Thus, the aim of this investigation was to assess the photocatalytic activity of the MZC nanocomposite towards the photodegradation of MB. The efficiency of the MZC nanocomposite was also evaluated for industrial wastewater collected from KK textile industry located at Addis Ababa, Ethiopia. The results show the potential application of the MZC nanocomposite for effective textile dye degradation.

2. Experimental part

2.1. Chemicals and materials

Chemicals and reagents, including $(C_4H_6O_2)_n$, 99.9%; $KMnO_4$, 98.5%; $MnSO_4 \cdot H_2O$, ≥99.00%; and NaOH, 97.00%, were purchased from Merck, India. $Zn(CH_3COO)_2 \cdot 2H_2O$, 99.9%; $HgSO_4$, 99.98%; Ag_2SO_4; $AgNO_3$, 99.5%; $K_2Cr_2O_7$, 99.5%; $NaHCO_3$, 99%; CH_3OH, 99.85%; and $Cu(NO_3)_2 \cdot 3H_2O$, ≥99%, were obtained from Sigma-Aldrich. Every chemical was of research-grade. Distilled water (DW) was employed for dissolving and cleaning the impurities in the study.

2.2. Preparation of samples

2.2.1. Preparation of the pristine Z, M and C photocatalysts. The Z nanoparticles were prepared *via* a method developed previously.[37] Prior to this, 0.02 g of $Zn(CH_3COO)_2 \cdot 2H_2O$ was added in the mixed 50 : 25 mL ratio of DW and CH_3CH_2OH. Then, 0.2 M solution of NaOH was prepared and added to the solution containing $Zn(NO_3)_2 \cdot 6H_2O$ until a white precipitate was formed. The subsequent suspensions were settled down after 9 h, and undesired impurities were removed by washing with DW and CH_3CH_2OH. The sample was dried at 100 °C and then calcined at 420 °C to attain the desired Z nanoparticles. By the same method, the M and C photocatalysts were synthesized using the corresponding metal precursors, except potassium permanganate was added to prevent Mn oxidation during the preparation of the pristine M catalyst.

2.2.2. Preparation of the PVA-supported MZC composite. The MZC nanocomposite was prepared *via* a method modified by B. Abebe *et al.*[37] Typically, solutions A, B, and C were prepared by dissolving 5% of $Cu(NO_3)_2 \cdot 3H_2O$, 90% of $Zn(NO_3)_2 \cdot 6H_2O$, and 5% ($KMnO_4$ and $MnSO_4$) with distilled water (DW) in separate beakers, respectively (Scheme 1). Potassium permanganate was added into solution C to prevent Mn oxidation. The three solutions were mixed in another beaker. NaOH was added to the mixed solution until the pH level reached 12. 1.8 g of PVA was dissolved in boiled DW and stirred at 100 °C for 15 min (solution D). The product solutions (such as A, B, and C) were added into solution D after cooling the PVA solution. The mixture solution was then allowed to settle for a period of two days, after which it was separated by centrifugation. It was then washed several times with DW and CH_3CH_2OH, dried, and calcinated at 100 °C and 420 °C.

2.3. Characterizations

The prepared nanocomposites were examined using DTA (DTG, 60 H, and Shimadzu Japanese) to ascertain the thermal stability of the samples. With a scanning rate of 10 min^{-1} and a Cu Kα radiation ($\lambda = 0.154\,060$ nm) source, the phase composition and crystallite size of the prepared samples were evaluated using XRD (XRD-7000, Shimadzu, Japan) in the 2-theta range of 20° to 80°. Diffuse reflectance spectroscopy (DRS) of all composite materials was conducted (JASCO.V-770, Shimadzu, Japan) in the

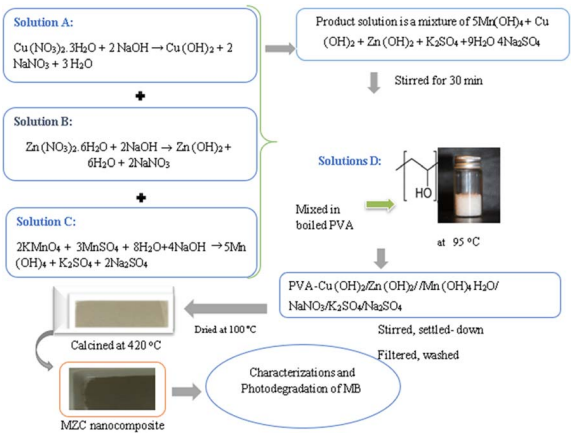

Scheme 1 Schematic showing the preparation of the MZC nanocomposite photocatalyst.

wavelength range between 200 and 800 nm. The morphological shapes of the manufactured nanocomposites were explored *via* scanning electron microscope (JSM 6390 L V, JEOL, Japan). The surface structure of the triple-phase components was explored through electron microscopy (SEM) equipment, and the elemental composition of the composites was determined with EDS. Likewise, using TEM and HRTEM (JEOL JEM 2100, Japan), the internal structures of the prepared MZC heterojunction were studied.

2.3.1. Catalytic performance test. Under visible light irradiation, the catalytic potential of the as-prepared nanomaterials towards the photodegradation of MB dyes was examined. Each degradation experiment was conducted at ambient temperature. In a beaker, by changing the amount of the synthesized photocatalyst load, the initial MB concentration, and the pH value, the efficiency of the catalyst was optimized. Mixed aqueous solutions of MB (10, 15, 20, 25, 30, 35 mg in 100 mL) and catalyst load (50, 70, 90, 110, 130, 150 mg in 100 mL) were added to a beaker in the dark and stirred. The pH values in the range between 2 to 12 were adjusted by an acid–base reaction for the resulting solution. Before illumination, the mixture was stirred in the dark to achieve equilibrium between adsorption and desorption. Then, in the photoreactor setup, the system was exposed to visible light using a 60 W LED lamp manufactured by Havells, India. The distance between the solution and the lamp was consistently set at 12 cm. Air was forced into the solution using porous tubes with a controlled flow rate, while the sample was exposed to visible light. After that, 5 mL of sample was taken out every 20 min. Before measuring the absorbance, the catalyst particles were removed by centrifuging and filtering the mixture. A UV-vis spectrophotometer was used to estimate the % degradation, rate constant, and the removed MB concentration at 665 nm with eqn (1) and (2):

$$\%\ \text{degradation} = (C_0 - C)/C_0 \text{ or } (A_0 - A)/A_0 \times 100 \quad (1)$$

$$\ln(C_0/C) = k_{ap}t \quad (2)$$

where C_0 is the initial dye concentration, C is the concentration of dye at irradiation time t, A_0 is the dye's initial absorbance before irradiation, A is the absorbance of the dye at the irradiation time t, and k_{ap} is the apparent pseudo-first-order rate constant.

2.3.2. Industrial real sample analysis. In this study, some physicochemical properties (like turbidity, pH, and COD content) of the industrial wastewater collected from KK textile factory were assessed. To determine the COD content, different 0.25 M solutions of $K_2Cr_2O_7$ and 0.50 M solutions of H_2SO_4 were prepared using DW. The water sample was collected and separated by centrifuging to remove any suspension of solid materials. Then, 25 mL of the separated solution was digested in the digestion vial. The Ag_2SO_4 solution was used as a catalyst to facilitate the oxidation reaction. A certain dissolved amount of $K_2Cr_2O_7$ solution and the real sample were mixed together. Then, the H_2SO_4 solution was placed in a vial through stirring for completing digestion. After completing the digestion, the sample was stored in a CR 4200 COD reactor for 2 h at 152 °C to encourage the oxidation reaction of carbon-based dyes. The vial sample was cooled at room temperature by mixing *via* reversing for the COD concentration estimation. The levels of COD present in the textile wastewater were assisted by the COD detector. For plotting the calibration curve to calculate the COD level of MB in the textile wastewater, standard solutions were prepared with known COD contents.

2.3.3. Recyclability of the catalyst. One significant concern for practical use in processes of degradation is the reuse of the photocatalyst nanomaterials. To accomplish this, MB was photodegraded over the selected synthesized MZC composite in a series of cycles under visible light irradiation by collecting and recycling the photocatalyst. The synthesized composite was decanted and washed repeatedly with ethanol and distilled water.

3. Results and discussion

3.1. Characterizations

3.1.1. Thermal analysis. The thermal property of the MZC nanocomposite was studied by TGA-DTA (Fig. 1). The weight loss for the MZC nanocomposite is 12.61%. This loss is probably a result of water loss, which starts at ambient temperature. Moisture continues to be removed until 420 °C for the MZC nanocomposite. Two exothermic reactions are observed in the nanocomposites, as illustrated in the DTA results (Fig. 1). Moreover, the endothermic process against the composite was witnessed by the breakdown of the metal nitrate and sulfate. A broad and sharp downward peak also shows a dehydration reaction and the variation of crystallinity for the as-synthesized materials. After the endothermic process, the temperature reaches a minimum and is thermodynamically constant owing to the completion of decomposition. Thus, 420 °C was selected for calcining the synthesized composites based on the mentioned result.

3.1.2. XRD diffraction. The single phase of the Z, M, and C photocatalysts, and the mixed phases of the MZC nanocomposite were characterized by XRD (Fig. 2). The diffraction

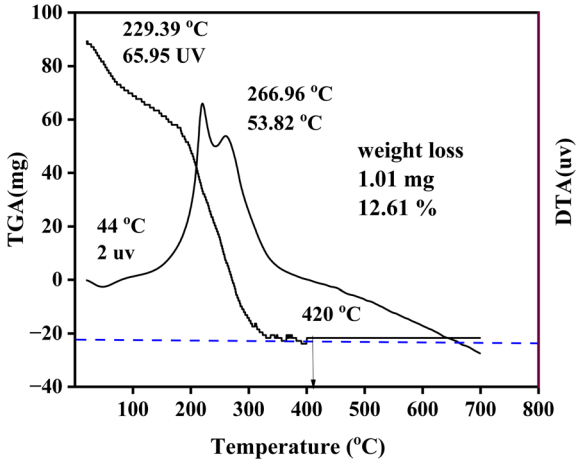

Fig. 1 Thermal analysis of the MZC heterojunction nanocomposites.

peaks obtained at 2θ = 31.94°, 34.56°, 36.42°, 47.64°, 56.77°, 62.94°, 66.34°, 68.04°, 69°, 72°, and 77° are matched to the (*hkl*) planes (100), (002), (101), (102), (110), (103), (200), (112), and (201), respectively, and represent the hexagonal wurtzite structure of Z (card number: 00-062-0414) with $P6_3mc$ (186) space group. The 2θ values with Miller indexes of 12.7° (110), 17.9° (200), 28.7° (310), 37.5° (211), 41.9° (301), 49.7° (411), and 60.1° (220) substantiate the formation of the M photocatalyst. The 2θ values with Miller indexes of 32.6° (002), 35.6° (111), 38.2° (020), 48.9° (200), 53.6° (022), 58.4° (113), 61.6° (311), 65.9° (222), 66.3° (202), 68.1° (220), 72.5° (004) and 75.40° (331) represent the monoclinic structure of C. In the MZC nanocomposite, the four diffraction peaks with planes at 28° (110), 37° (101), 47° (111), and 72° (301) verify that M has a cubic structure in the mixed materials. The 2θ values of roughly 35°, 38°, 43°, 48°, 53°, 61°, 68°, and 72° with the matching Miller indexes of ($\bar{1}$11), (111), (200), (020), (202), ($\bar{1}$13), (311) and (222) were observed. This indicates the presence of a monoclinic shape for C in the synthesized materials. All diffraction peaks located in the MZC nanomaterials are identified as those for the MnO_2, CuO, and ZnO photocatalysts. The recorded XRD findings indicate the formation of the heterojunction (coexistence of Zn, Cu, and Mn-oxides in a nanocomposite).

$$D = k\lambda/\beta \cos\theta \quad (3)$$

where D is the crystallites' size, k is the Scherrer's constant depending on the shape of the particles (0.94), λ is the wavelength of the X-ray radiation (0.15418 nm for Cu Kα), β is the full width at half maximum (FWHM) intensity (in degree, which is converted to radian), and θ is the diffraction (Bragg) angle. According to the analysis, the estimated average crystalline sizes of the Z, M, C and MZC materials are 37.05, 43.5, 29.01, and 26.04 nm, respectively. The average size of the MZC composite is 0.7, 0.59, and 0.89 times that of the Z, M, and C photocatalysts, respectively. The results indicate the presence of size modification when pristine materials combined.

3.1.3. Surface morphology. SEM-EDS, EDS elemental mapping, and HRTEM were used to study the morphology and elemental analysis of the composites. Fig. 3a–d shows the SEM images of the single phase Z, M, and C photocatalysts, and the mixed phases of the MZC nanocomposites. The SEM images of the as-synthesized nanomaterials were obtained by scanning the samples with a beam of electrons.[39] The SEM results for Z, M, and C indicate a spherical shape with an aggregated

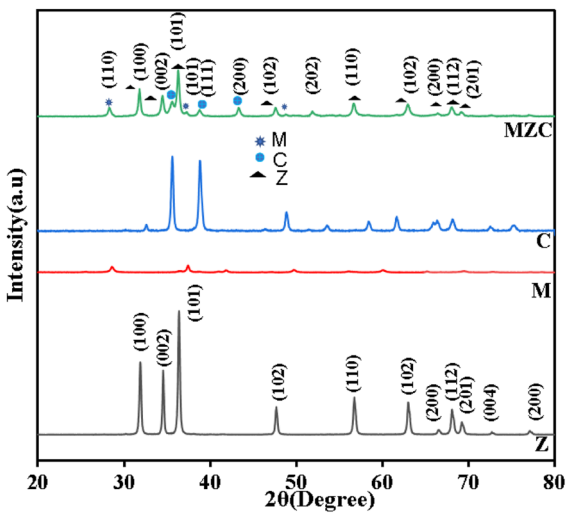

Fig. 2 XRD diffraction patterns of the Z, M, C, and MZC nanocomposites.

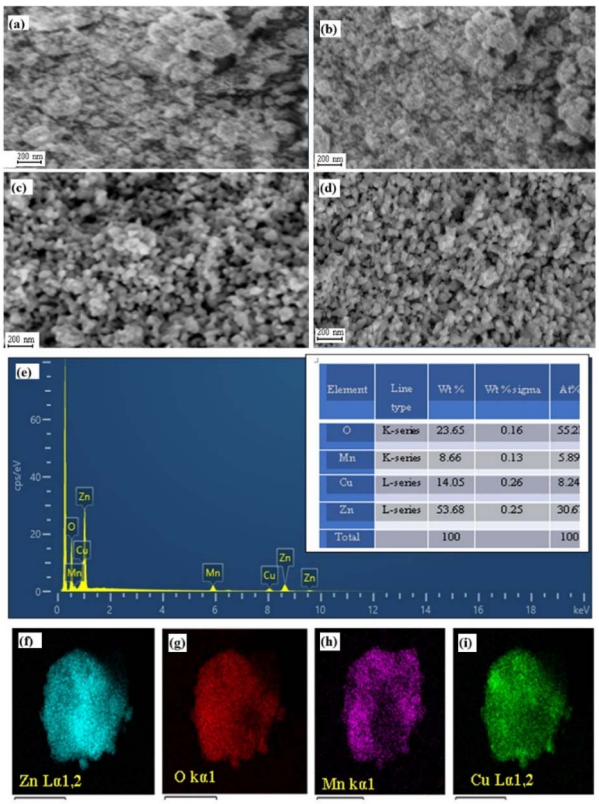

Fig. 3 SEM image of (a) Z; (b) M; (c) C; and (d) MZC. (e) EDS elemental composition; and Elemental mapping of (f) Zn; (g) O; (h) Mn; and (i) Cu.

framework (Fig. 3b). The SEM image of MZC also reveals a uniformly distributed spherical shape with non-agglomerated structures (Fig. 3d). This may be due to the strong binding ability of polyvinyl alcohol. The elemental composition and mapping of the MZC nanocomposite are shown in Fig. 3e. The anticipated elements, such as O, Zn, Mn, and Cu, were found to have relative weights of 23.65, 53.68, 8.66, and 14.05%, respectively (Fig. 3e inset). The EDS spectrum of the MZC nanocomposite sample exhibits signals ascribed to the Zn, Cu, Mn, and O elements. The results demonstrate that there were no impurities present in the prepared MZC nanocomposite. The EDS elemental mapping confirms the existence of expected elements, such as Zn, Mn, Cu, and O, in the prepared nanomaterial (Fig. 3f–i).

The TEM result shows the presence of spherical C and cubic M photocatalysts loaded on the surface of Z, as shown in Fig. 4a. These photocatalysts are arranged favorably without aggregation (Fig. 4a). For additional evaluation, the internal morphology of the M nanocomposite was studied, as presented in the HRTEM image. The HRTEM image (Fig. 4b) shows that the M composite has a wurtzite, spherical, and cubic structure without any agglomeration. From the histogram, the predicted diameter is 27 nm (Fig. 4d). This result is consistent with the value obtained from XRD. The predicted lattice fringe *d*-spacing from HRTEM is 0.238, which is ascribed to the M (211) plane. Also, the interplanar spacing values are 0.246, 0.259, and 0.283 nm, and ascribed to Z(101), (100), and (002), respectively. Additionally, a *d*-spacing of 0.221 nm was estimated and attributed to C (111). The obtained results reveal the effective creation of a heterojunction. The stacking faults on the Inverse Fast Fourier Transform (IFFT) analysis signify the crystalline nature of the material (Fig. 4b inset). The selected area electron diffraction (SAED) revealed the presence of different concentric circles with the same center assigned to the (100), (002), and (101) planes of hexagonal Z, in addition to the (111) and (211) planes of cubic M and spherical C nanoparticles (Fig. 4c).

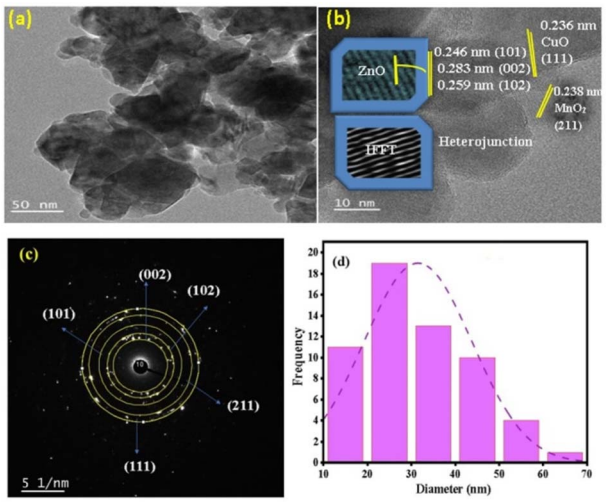

Fig. 4 (a) TEM, (b) HRTEM analysis, (c) SAED, and (d) particle size of the MZC nanocomposite.

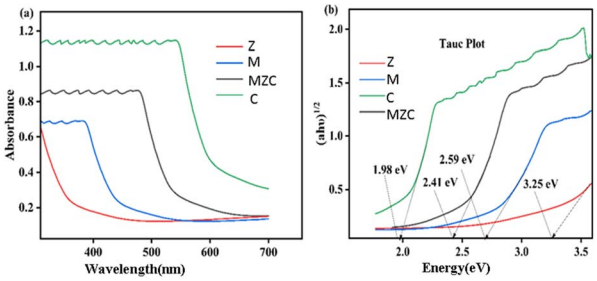

Fig. 5 (a) UV-vis analysis and (b) Tauc plot of the Z, M, C, and MZC nanomaterials.

3.1.4. DRS analysis. The light absorbance properties of the Z, M, and C photocatalysts were examined using UV-vis diffuse reflectance spectroscopy (DRS). The Z photocatalyst demonstrated the ability to absorb light within the ultraviolet (UV) wavelength range. In contrast, the M and C photocatalysts demonstrate light absorption in the visible region, as illustrated in Fig. 5a. The Z sample exhibits a higher absorption rate for shorter wavelengths than the M, C, and MZC nanocomposites. Conversely, the C sample demonstrates a higher absorption rate for longer wavelengths than the Z and M samples. The MZC nanocomposite displays a higher absorption rate for long wavelengths, indicating that the band edge modification of Z, when coupled with the M and C photocatalysts, exhibits enhanced optical properties.

The band gap energy of the synthesized samples was also estimated from the Tauc plot $(\alpha h\nu)^{n/2}$ *versus* $h\nu$, where α is the optical absorption coefficient, $h\nu$ is the energy of a photon, E_g is the band gap, and n is the transition type of a semiconductor (its value is 1 or 4 for direct and indirect, respectively). The direct band gap of the as-prepared materials was estimated from a plot of $(\alpha h\nu)^{1/2}$ *versus* $h\nu$ (Fig. 5b). Accordingly, the calculated band gaps for Z, M, C, and MZC were found to be 3.25 eV, 2.59 eV, 1.98 eV, and 2.41 eV, respectively. The findings revealed that all as-prepared samples exhibited UV-visible absorption, with the exception of Z. In general, the Z photocatalyst exhibited a shift from hypsochromic to bathochromic when forming a nanocomposite. This enhanced visible light absorption of the MZC nanocomposite photocatalyst suggests the potential for effective photocatalytic degradation reactions under various conditions.

3.2. Photocatalytic activity test

The photocatalytic efficiency of the MB, Z, M, C, and MZC materials *versus* the MB dye was evaluated under visible light radiation within 180 min (Fig. 6a and b). The mixed aqueous solution of 130 mg catalyst load and 10 mg MB was employed for all samples. Adsorption–desorption processes typically occurred during the investigation in dark (light off) and bright (light on) conditions. In the dark, the % degradation is almost the same and low for all materials because of the slow reaction rate. Moreover, the reaction rate and % degradation for all of the as-synthesized nanomaterials increased after dark (light off) conditions (Fig. 6a and b).

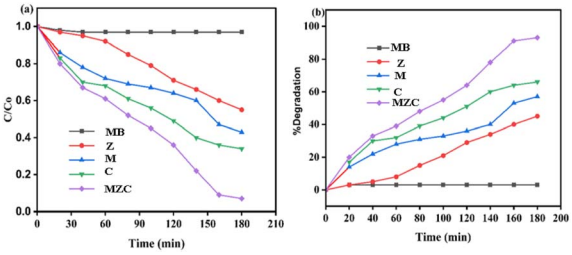

Fig. 6 (a) C/C_0 *versus* irradiation time, (b) % degradation *versus* irradiation time using 10 mg MB and 130 mg of the Z, M, C, and MZC samples.

Each material (such as MB, Z, M, C, and MZC) exhibited a maximum photodegradation efficiency of 3%, 45%, 57%, 66%, and 93%, respectively (Fig. 7b). Conversely, from 0 to 180 min, the MB concentration decreased, which prompted an increment in the degradation rate (Fig. 7b). An insignificant degradation efficiency of MB was observed, as indicated in Fig. 7a and b. The efficiency of Z was lower than those of other materials (Fig. 7b). The increasing order of degradation efficiency may be a result of the lowering band gap in that respective order.[21] Furthermore, the MZC composite exhibited outstanding catalytic performance.

3.2.1. Effect of the pH solution and point zero charge. One significant parameter that needs to be optimized for subsequent experiments is the pH value. In this study, the MZC nanocomposite was selected for optimization of the pH value due to it being the uppermost efficient material among the as-synthesized samples. Hence, photocatalytic degradation experiments were carried out using different pH levels, including pH = 2, 4, 6, 8, 10, and 12 (Fig. 7a–d). We used 130 and 10 mg of photocatalyst load and MB content, respectively, to conduct this study. The MB concentration decreases with increasing pH solution from 2 to 8. Beyond the pH value of 8, the MB degradation decreases (Fig. 7a and b). The highest % degradation of MB at pH values of 2, 4, 6, 8, 10, and 12 are 56.1%, 60.5%, 85%, 93%, 78%, and 75%, respectively, as indicated in Fig. 7c. These findings demonstrate that the degradation efficiency increased from 56.1% to 93% as the pH value increased from 2 to 8. However, the MZC degradation efficiency decreased from 78% to 75% between pH 10 and 12. The pH value of 8 was shown to be the optimal condition (Fig. 7b). 130 mg of M degraded 93% of 10 mg of MB. The low efficiency at the other pH conditions probably can be attributed to the low production of hydroxyl ions to generate reactive hydroxyl radicals.[7] The point zero charge was also studied to identify the surface charge of the MZC heterojunction nanocomposites using hydrochloric acid and sodium hydroxide solution to control the pH values. After the investigation was carried out, the point zero charge was 6.2 (Fig. 7d). The observed result indicates the presence of negative charges on the composite surface due to the pH being greater than 6.2 (point zero charge). After pH 8, the surface of the synthesized nanocomposite becomes negatively charged and the cationic MB dye can be adsorbed on the catalyst surface (Scheme 2). As a result of this adsorption of the MB dye on the nanocomposite surface, the degradation performance of the MB dye decreases. We found that the degradation of the MB dye was maximized at the pH level of 8. Based on this finding, we decided to concentrate our experiments at this optimal pH to enhance the degradation potential.

3.2.2. Impact of the initial dye concentration. The optimized pH value and 130 mg of the MZC catalyst load were taken to study the effect of MB concentrations in between 10 and 35 mg (Fig. 8a and b). The highest percentage (%) removal of MB at concentrations of 10, 15, 20, 25, 30, and 35 mg were 93%, 78.1%, 74.2%, 69.5%, 62.3% and 58%, respectively. This indicates that the degradation percentage is higher at lower MB concentrations (Fig. 8a and b). The highest degradation was obtained at the lowest initial dye of MB. The % degradation decreased from 93% to 58% when the dye content was increased from 10 to 35 mg. This is because the high content of dye hinders the penetration of photons, and decreases the production of a large number of reactive species on the catalyst surface.[33] The presence of a higher content of MB dye molecules in the reaction system may impede the photon light from reaching the composite's surface. Thus, this would result in a lower overall degradation efficiency of MB, as the

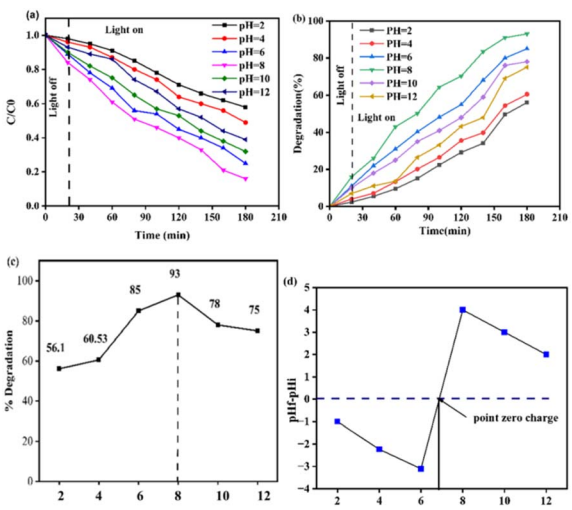

Fig. 7 (a) Concentration *vs.* radiated time at different pH values, (b) % degradation *vs.* irradiated time, (c) % degradation *vs.* pH, and (d) point zero charge of the M nanocomposites using 130 mg MZC and 10 mg MB.

Scheme 2 Indication of the surface charge of MZC on MB.

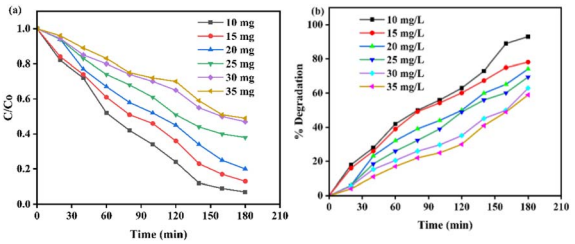

Fig. 8 (a) Plot of the MB concentration ratio *vs.* radiated time, and (b) % degradation *vs.* time irradiation by keeping constant the quantity of MZC (130 mg) and varying the MB solution.

nanocomposite catalysts are not able to fully utilize the incident light for the photodegradation process.

3.2.3. Effect of the photocatalyst load. The effects of various photocatalyst loads (such as 50, 70, 110, 130, and 150 mg) towards the degradation of 10 mg MB were investigated for a duration of 180 min with a pH value of 8. The highest concentration of MB was removed at 130 mg catalyst load (Fig. 9a). Moreover, 130 mg of MZC degraded 93% of 10 mg of MB dye (Fig. 9b). The highest % degradation for 50, 70, 110, 130, and 150 mg was 53%, 65%, 76%, 80%, 93% and 86%, respectively, as indicated in Fig. 9b. This is a paramount technique for choosing the most efficient material for various photocatalyst loads. According to the data obtained, the maximum degradation efficiency of MZC was 93%. The degradation efficiency for the other loads was lower. This indicates that increasing the photocatalyst load increases the photocatalytic efficiency up to the optimum load, and then decreases beyond the optimal load.[20] This is due to the presence of a large surface area as the loading of photocatalysts increased until the optimal photocatalyst load value was reached.[40] Particularly, the decrease of the photocatalytic efficiency was observed after a 130 mg load, which is ascribed to the shielding effect of the suspended particles from light penetration into the MZC solution. Therefore, 130 mg of the photocatalyst was chosen as the optimum catalyst load for the remaining experimental studies, as it was most effective for photocatalytic enhancement.

3.2.4. Mechanism of photodegradation. The roles of reactive species, such as superoxide radical ($^{\bullet}O_2^-$), electron (e^-), hole (h^+), and hydroxyl radical ($^{\bullet}OH$), were evaluated by employing their respective scavengers in the proposed mechanism for the photocatalytic degradation of MB over the MZC nanocomposite under the optimum conditions. In this study, various scavengers such as $C_{15}H_{24}N_2$ for e^-, $AgNO_3$ for $O_2^{\bullet-}$, CH_3OH/OH for $^{\bullet}OH$, and $NaHCO_3$ for h^+ were employed. The photocatalytic degradation of MB in the presence of scavengers is illustrated in Fig. 10a and b. At optimal conditions, the MZC nanocomposite degraded 93% of MB. However, the degradation capacity of the MZC nanocomposite was observed to be 58.5%, 36%, 48.5%, and 32.5%, respectively, when the $AgNO_3$, $C_{15}H_{24}N_2$, CH_3OH, and $NaHCO_3$ scavengers were employed (Fig. 10b). This outcome demonstrates the involvement of the $^{\bullet}O_2^-$, e^-, h^+, and $^{\bullet}OH$ reactive species in the degradation processes. However, it is notable that substantial involvement of h^+ and $^{\bullet}OH$ is observed in the degradation of MB.[40]

To elucidate the excited charge separation in the MZC nanocomposites, the conduction band (CB) and valence band (VB) edges were calculated for each photocatalyst by employing the equations: $E_{CB} = x - E - 0.5E_g$ and $E_{VB} = E_{CB} + E_g$,[15] where E_{VB} is the valence band edge potential, x is the absolute electronegativity of the semiconductor, E is the energy of free electrons on the hydrogen scale (4.5 eV), E_g is the band gap energy, and E_{CB} is the conduction band edge potential. The calculated E_g values for the ZnO, MnO_2, and CuO catalysts are 3.25 eV, 2.59 eV and 1.98 eV, respectively. The E_{VB} and E_{CB} values of ZnO, MnO_2, and CuO are also estimated to be 2.90, 2.76, 2.26, and −0.34, 0.165, and 0.34 eV, respectively. The generation of h^+/e^- occurs in the VB and CB of each component when the MZC heterojunction nanocomposite interacts with visible light. The electron affinity of ZnO is more negative than that of CuO and MnO_2. Similarly, the E_{VB} of ZnO is more positive than that of CuO and MnO_2. If the migration pathway of

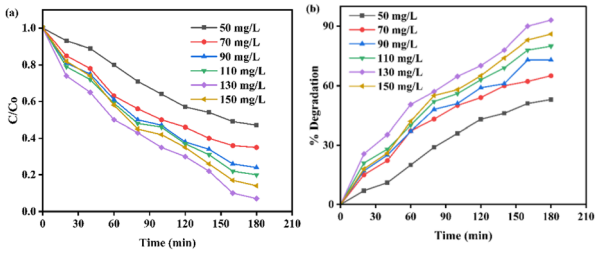

Fig. 9 Plots of the (a) MB concentration ratio *vs.* time and (b) % degradation *vs.* irradiation time with different MZC loads, while keeping constant the quantity of MB and the pH level.

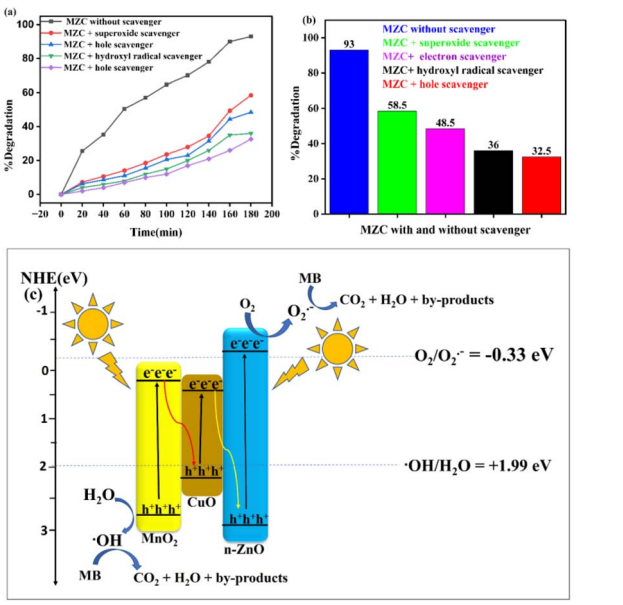

Fig. 10 (a and b) Effect of scavengers on the photocatalytic activity of the MZC heterojunction nanocomposite; (c) proposed mechanism for the MZC heterojunction nanocomposite under visible-light radiation.

charge carriers generated during the photocatalytic processes follows the type-II heterojunction, then electrons generated in the E_{CB} of MnO_2 and ZnO can be transferred to CuO, and holes generated in the E_{VB} of MnO_2 and ZnO can be transferred to CuO. In this case, the E_{VB} of CuO (+2.26 eV) is more positive than the potential of $^{\bullet}OH/H_2O$ ($E^{\circ} = +1.99$ eV),[38] indicating that the holes at the EVB of CuO possess sufficient oxidizing ability to oxidize H_2O or OH^- to form $^{\bullet}OH$. However, the electrons at the E_{CB} of CuO are unable to reduce O_2 to $^{\bullet}O_2^-$ due to the fact that the E_{CB} of CuO (+0.34 eV) is more positive than the $O_2/^{\bullet}O_2^-$ ($E^{\circ} = -0.33$ eV).[15] This is in contradiction with the results obtained from the active species trapping experiments (Fig. 10a and b). It became evident that the type-II heterojunction mechanism was not an appropriate fit for the MZC nanocomposite photocatalytic system. Accordingly, the Z-scheme system is a logical representation of the enhanced photocatalytic activity observed in the MZC nanocomposite, as illustrated in Fig. 10c. In this instance, the generated electrons in the E_{CB} of MnO_2 are prone to transfer and recombine with the holes in the E_{VB} of CuO, driven by the internal electric field at the junction between these. Similarly, the excited electrons in the E_{CB} of CuO are transferred and recombine with the holes in the E_{VB} of ZnO. These electron–hole transfer and combination processes result in the accumulation of electrons in the E_{CB} of ZnO and holes in the E_{VB} of MnO_2. Consequently, the generated electrons in the E_{CB} of ZnO can readily reduce O_2 to generate the $^{\bullet}O_2^-$ reactive species. Concurrently, the accumulated holes in the E_{VB} of MnO_2 can directly engage in the MB degradation process or oxidize H_2O to yield the $^{\bullet}OH$ active species. This mechanism aligns with the outcomes of the reactive species detection experiments. Therefore, the Z-scheme photocatalytic system of the MZC nanocomposite facilitates not just the transfer and separation efficiency of the generated electron–hole, but also preserves the robust redox capability in the photodegradation process.

3.2.5. Recyclability of the catalyst. The MZC nanocomposite was selected to evaluate its permanence because of its high efficiency. After the photocatalytic degradation process took place, the recyclability of the MZC catalyst was explored by washing it with ethanol and distilled water several times and oven-drying at 60 °C to remove undesired impurities from the MZC catalyst. Next, the photocatalytic activity was carried out using a catalyst load of 130 mg and 10 mg of MB over a period of 180 min. Using the same procedures, four series of experiments were carried out, and no visible change in the degradation efficiency was observed, as illustrated in Fig. 11a. The result was verified by characterizing the composite with XRD and FTIR after the fourth cycle (Fig. 11b and c). The investigation revealed that despite being used for the fourth sequential photodegradation reaction, the composite's phase composition and functional groups remained almost the same. This is probably due to the structural stability of the composite.

3.3. Industrial wastewater analysis

Some significant physicochemical properties, such as the turbidity, pH, and COD, were explored before wastewater treatment from the KK textile factory. According to the World Health Organization (WHO), the suitable pH range was found to be in the range of 6.5 to 8.5 and 6 to 9 for aquatic organisms and human beings, respectively.[41] Unfortunately, the pH value of 8 was the optimal condition during the photocatalytic degradation of MB, and we employed pH 8 for our experiment. Another crucial feature of textile wastewater is turbidity, which prevents the penetration of light and oxygen transfer processes in water bodies, and results in the disturbance of living organisms. Hence, textile wastewater needs to be treated before being discharged into the surface water. In our case, 90% to 98% removal was achieved with an average of 94%.

The present work was also carried out to determine the concentration of COD in industrial waste collected from KK

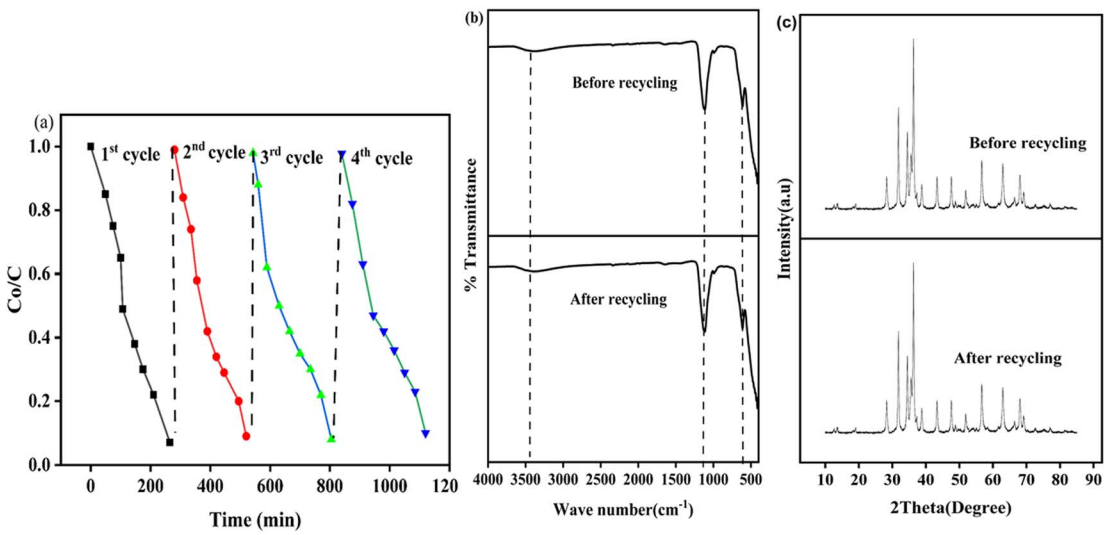

Fig. 11 (a) Reusability of the MZC nanocomposite photocatalyst after four successive runs; (b) FTIR spectra of the MZC nanocomposite before and after recycling; (c) XRD diffraction of the MZC nanocomposite before and after recycling.

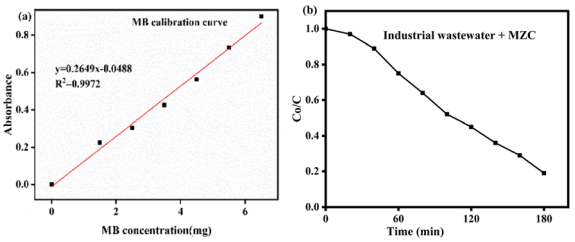

Fig. 12 Plots of the (a) MB calibration carve and (b) industrial wastewater treatment.

Textile Factory. The estimated concentration of COD from textile wastewater was in the range of 22–235 mg. This value is similar to the value reported by Hussein and Scholz,[42] and Yaseen and Scholz.[43] Nevertheless, many researchers reported the presence of a higher concentration of COD in textile factories. For instance, Verma *et al.*,[44] Aouni *et al.*,[45] Aldoury *et al.*,[46] Mountassir *et al.*,[47] and Punzi *et al.*[48] reported 770–790, 450–566, 650–900, 736 mg, and 590 mg of COD concentrations, respectively. This higher COD concentration shows the presence of numerous contaminants in wastewater. Before estimating the efficacy of the MZC composite, it is important to determine the COD value of MB in industrial wastewater using a calibration curve. The curve is a plot of the absorbance of a series of standard solutions with various content of MB, such as 0.00, 1.5, 2.5, 3.5, 4.5, 5.5, and 6.5 mg (Fig. 12a). The absorbance values for the respective concentrations were 0.00, 0.225, 0.305, 0.425, 0.565, 0.735, and 0.9015, respectively. From these data, the unknown COD concentration of MB was estimated to be 13.69 mg. The concentration of reactive dyes in the textile industry has been reported in various studies. M. F. Abid *et al.*[49] reported a concentration range of 10–50 mg. However, N. Koprivanac *et al.*[50] reported an extremely high concentration of 7000 mg, which may be ascribed to the sewage release from a specific textile industry. On the other hand, V. V. A. E. Ghaly *et al.*[18] revealed that the released dye content ranged from 10 to 250 mg.

It is important to note the significant variation in the reported concentrations, which can be attributed to different textile industry practices and effluent treatment processes. The absorbance of the sample was compared to the calibration curve to determine the unknown concentration of MB from the real sample. Afterward, the catalytic efficacy of the prepared composite was investigated under visible light radiation (Fig. 12b). The prepared material degraded 80% of the pollutants from the real sample. This result reveals that the efficiency of MZC on the real sample was good, and it is in good agreement with previous work reported by T. Hail and coworkers[21] and A. Tadesse and his research group.[7] The degradation efficiency of the MZC heterojunctions using industrial wastewater and synthetic MB was compared. The result indicates that the photodegradation performance of MZC towards the real sample is lower than that of MB. That means the efficiency of the MZC heterojunction nanocomposite in degrading synthetic MB dye was two-fold higher compared to its efficiency in degrading textile wastewater. The decreasing performance of the wastewater condition might be ascribed to the nature of the sewage; it is a mixture of numerous dyes and other chemicals used through coloring. Nonetheless, the MZC heterojunction is an efficient and capable material for the removal of dye from real samples.

4. Conclusion

In this study, single phase Z, M, C photocatalysts, and MZC nanocomposite were synthesized by the sol–gel method. TGA-DTA analysis was used to determine the calcination temperature (420 °C) for the synthesized samples. The crystalline composition or size, band gap energy, and morphological characteristics of the synthesized photocatalysts were also characterized using XRD, DRS, SEM, EDS, TEM, HRTEM, and SAED to confirm the formation of heterojunction photocatalysts. The photocatalytic performance of the synthesized photocatalysts was explored for the photodegradation of the MB dye. The outcomes of the study confirmed that the ternary nanocomposite exhibited superior photocatalytic activity compared to its counterpart. The efficiency of dye removal is influenced by several factors, such as the pH levels, initial dye content, catalyst loads, and different scavengers. The maximum (93%) dye removal was achieved at a pH of 8, 10 mg of initial dye concentration, and 130 mg of catalyst load. Furthermore, the photocatalytic activity of the synthesized nanocomposites using electron, hole, superoxide free radical ion, and hydroxyl ion was carried out. The recyclability of the nanocomposites was also investigated. It was found that they maintained relatively stable photocatalytic activity after four cycles, indicating their potential for practical application in wastewater treatment. The photocatalytic performance of the industrial wastewater was also studied. The synthesized MZC nanocomposite degraded 80% of the industrial wastewater. These findings contribute to the development of efficient and sustainable water treatment technologies, addressing the pressing issue of dye pollution in wastewater. Further research can be explored for optimizing the synthesis parameters, investigating other dye pollutants, and scaling up the nanocomposites for real-world applications.

Data availability

The data supporting this article have been included as part of the ESI.†

Author contributions

T. G. G.: methodology, data analysis, and writing of the manuscript draft. T. B. A.: supervision, methodology, resources. G. G.: revision, software, editing. T. D. H.: methodology, analysis, revision. T. G. A.: methodology, analysis, revision. F. M.: revision, software, editing. E. A. Z.: supervision, conceptualization, analysis, revision.

Conflicts of interest

There are no conflicts to declare.

Acknowledgements

The present study is supported by Wolkite University and Addis Ababa Science and Technology University. Our group is also thankful to Addis Ababa and Adama Science and Technology universities for providing support with the microstructure characterization. The authors would also like to thank Scientific Compass (Hangzhou Yanqu Information Technology Co., Ltd) for surface analysis.

References

1 A. Momeni, M. H. Meshkatalsadat, B. Bakhtiari Shahin and Y. Mousavi, *Hybrid Adv.*, 2023, **3**, 100050.
2 A. Negash, S. Mohammed, H. D. Weldekirstos, A. D. Ambaye and M. Gashu, *Sci. Rep.*, 2023, **13**, 1–12.
3 D. Abdrabou, M. Ahmed, A. Hussein and T. El-Sherbini, *Environ. Sci. Pollut. Res.*, 2023, **30**, 99789–99808.
4 M. Abdullah, P. John, Z. Ahmad, M. N. Ashiq, S. Manzoor, M. I. Ghori, M. U. Nisa, A. G. Abid, K. Y. Butt and S. Ahmed, *Appl. Nanosci.*, 2021, **11**, 2361–2370.
5 O. A. Saputra, M. D. Prameswari, V. T. D. Kinanti, O. D. Mayasari, Y. D. Sutarni, K. Apriany and W. W. Lestari, *Mater. Sci. Eng.*, 2017, 012039.
6 A. M. Taddesse, T. Bekele, I. Diaz and A. Adgo, *J. Photochem. Photobiol., A*, 2021, **406**, 113005.
7 T. Taddesse, A. M. Alemu and T. Kebede, *J. Environ. Chem. Eng.*, 2020, **8**, 104356.
8 W. Mohammed, M. Matalkeh, R. M. Al Soubaihi, A. Elzatahry and K. M. Saoud, *ACS Omega*, 2023, **8**, 40063–40077.
9 K. Zhao, Y., H. Lian, C. Tian, H. Li, W. Xu, S. Phuntsho and F. Shih, *Environ. Sci. Eng.*, 2021, **15**, 1–13.
10 D. G. Ayu, S. Gea, N. Andriayani, D. J. Telaumbanua, A. F. R. Piliang, M. Harahap, Z. Yen, R. Goei and A. I. Y. Tok, *ACS Omega*, 2023, **8**, 14965–14984.
11 Z. Yang, Y. Zhou, Z. Feng, X. Rui, T. Zhang and Z. Zhang, *Polymers*, 2019, **11**, 1–22.
12 L. Zhu, H. Li, P. Xia, Z. Liu and D. Xiong, *ACS Appl. Mater. Interfaces*, 2018, **10**, 39679–39687.
13 H. Abdo, K. Namratha, P. Deepalekshmi, Q. A. Drmosh, M. N. S. Adel, C. Chun and K. Byrappa, *ACS Omega*, 2018, **3**, 12260–12269.
14 S. Wang, B. Zhu, M. Liu, L. Zhang, J. Yu and M. Zhou, *Appl. Catal., B*, 2019, **243**, 19–26.
15 G. Gebreslassie, P. Bharali, U. Chandra, A. Sergawie, P. K. Baruah, M. R. Das and E. Alemayehu, *Appl. Organomet. Chem.*, 2019, **33**, e5002.
16 S. Ruan, W. Huang, M. Zhao, H. Song and Z. Gao, *Mater. Sci. Semicond. Process.*, 2020, **107**, 104835.
17 R. Saravanan, S. Karthikeyan, V. K. Gupta, G. Sekaran, V. Narayanan and A. Stephen, *Mater. Sci. Eng., C*, 2013, **33**, 91–98.
18 V. V. A. E. Ghaly, R. R Ananthashankar, M. Alhattab and J. Ramakrishnan, *Chem. Eng. Process Technol.*, 2013, **05**, 1–19.
19 Y. Wang, J. Gao, X. Wang, L. Jin, L. Fang, M. Zhang, G. He and J. Sun, *J. Sol-Gel Sci. Technol.*, 2018, **88**, 172–180.
20 C. Wang, H. Ni, J. Dai, T. Liu, Z. Wu and X. Chen, *Chem. Phys. Lett.*, 2022, **803**, 139815.
21 H. Tedla, I. Díaz, T. Kebede and A. M. Taddesse, *J. Environ. Chem. Eng.*, 2015, **3**, 1586–1591.
22 A. Taufik, A. Albert and R. Saleh, *J. Photochem. Photobiol., A*, 2017, **344**, 149–162.
23 L. T. Nguyen, L. T. Nguyen, A. T. Duong, B. D. Nguyen, N. Quang Hai, V. H. Chu, T. D. Nguyen and L. G. Bach, *Materials*, 2019, **12**, 1–11.
24 R. Singh, P. B. Barman and D. Sharma, *J. Mater. Sci.: Mater. Electron.*, 2017, **28**, 5705–5717.
25 W. Yu, J. Zhang and T. Peng, *Appl. Catal., B*, 2016, **181**, 220–227.
26 Z. Shao, Y. Wang, Y. Zhang, G. Zhu, X. Yang and M. Zhong, *J. Photochem. Photobiol., A*, 2018, **364**, 657–670.
27 J. P. Shubha, S. F. Adil, M. Khan, M. R. Hatshan and A. Khan, *ACS Omega*, 2021, **6**, 3866–3874.
28 A. Hezam, K. Namratha, Q. A. Drmosh, Z. H. Yamani and K. Byrappa, *Ceram. Int.*, 2017, **43**, 5292–5301.
29 D. C. Ashiegbu, N. Moloto and H. Potgieter, *Environ. Sci.: Adv.*, 2023, **2**, 1–26.
30 B. Li and Y. Wang, *Superlattices Microstruct.*, 2010, **47**, 615–623.
31 R. Renji, V. Shanmugam, S. Asokan, P. Palanisamy, S. Sanjeevamuthu, R. Vairamuthu, K. S. Jeyaperumal, S. Manickam, S. Mohd and S. AlFaify, *Colloids Interface Sci. Commun.*, 2021, **44**, 100480.
32 F. Mukhtar, T. Munawar, M. S. Nadeem, M. N. ur Rehman, M. Riaz and F. Iqbal, *Mater. Chem. Phys.*, 2021, **263**, 124372.
33 J. P. Shubha, H. S. Savitha, S. F. Adil, M. Khan, M. R. Hatshan, K. Kavalli and B. Shaik, *Molecules*, 2021, **26**, 4661.
34 S. Balachandran and M. Swaminathan, *J. Phys. Chem. C*, 2012, **116**, 26306–26312.
35 A. Habibi-Yangjeh and M. Shekofteh-Gohari, *Sep. Purif. Technol.*, 2016, **166**, 63–72.
36 B. Abebe, A. C. H. Murthy, Z. Enyew and A. Yeshaneh, *Mater. Res. Express*, 2020, **7**, 045011.
37 B. Abebe, C. H. M. Ananda, E. Zerefa and E. Abdisa, *Mater. Res. Express*, 2020, **7**, 1–16.
38 T. G. Gindose, T. B. Atisme, G. Gebreslassie, A. B. Gebresilassie and E. A. Zereffa, *Mater. Adv.*, 2024, **5**, 8017–8033.
39 B. Abebe, H. C. A. Murthy and E. A. Zereffa, *Res. Express*, 2020, **2020**, 1–14.
40 G. Gebreslassie, P. Bharali, U. Chandra and A. Sergawie, *J. Photochem. Photobiol., A*, 2019, **382**, 111960.
41 D. Tibebe, A. Negash, M. Mulugeta, Y. Kassa, Z. Moges and D. Yenealem, *BMC Chem.*, 2022, **16**, 1–9.
42 A. Hussein and M. Scholz, *Ecol. Eng.*, 2017, **101**, 28–38.
43 D. A. Yaseen and M. Scholz, *Environ. Sci. Pollut. Res.*, 2018, **25**, 1980–1997.
44 A. K. Verma, B. Puspendu and R. R. Dash, *Int. J. Chem. Nucl. Metall. Mater. Eng.*, 2012, **6**, 15–22.
45 A. Aouni, C. Fersi, B. Cuartas-Uribe, A. Bes-Pía, M. I. Alcaina-Miranda and M. Dhahbi, *Desalination*, 2012, **297**, 87–96.

46 M. M. Aldoury, W. M. S. Alabdraba, M. B. Al-bayati and J. Selçuk, *J. Selçuk Univ. Nat. Appl. Sci.*, 2014, 234–248.
47 Y. Mountassir, A. Benyaich, P. Berçot and M. Rezrazi, *J. Environ. Chem. Eng.*, 2015, **3**, 2900–2908.
48 M. Punzi, F. Nilsson, A. Anbalagan, B. M. Svensson, K. Jönsson, B. Mattiasson and J. Jonstrup, *Hazard. Mater.*, 2015, **292**, 52–60.
49 M. F. Abid, M. A. Zablouk and A. M. Abid-Alameer, *J. Environ. Health Sci. Eng.*, 2012, **9**, 1–9.
50 N. Koprivanac, G. Bosanac, Z. Grabaric and S. Papic, *Environ. Technol.*, 1993, **14**, 385–390.